

# Interannual variation of precipitation over the Hengduan Mountains during rainy season

Danhong Dong,<sup>a,b</sup> Gang Huang,<sup>a,b,c,d,\*</sup> Weichen Tao,<sup>a</sup> Renguang Wu,<sup>a,e</sup> Kaiming Hu<sup>a,e</sup> and Chaofan Li<sup>e</sup>

<sup>a</sup> State Key Laboratory of Numerical Modeling for Atmospheric Sciences and Geophysical Fluid Dynamics, Institute of Atmospheric Physics, Chinese Academy of Sciences, Beijing, China

<sup>b</sup> University of Chinese Academy of Sciences, Beijing, China

<sup>c</sup> Laboratory for Regional Oceanography and Numerical Modeling, Qingdao National Laboratory for Marine Science and Technology, China

<sup>d</sup> Joint Center for Global Change Studies, Beijing, China

<sup>e</sup> Center for Monsoon System Research, Institute of Atmospheric Physics, Chinese Academy of Sciences, Beijing, China

**ABSTRACT:** The present study investigates the interannual variability of precipitation over the Hengduan Mountains (HMs) during rainy season based on daily precipitation dataset of 151 meteorological stations. More HMs precipitation is associated with an anomalous lower level cyclonic circulation over the northern South China Sea (SCS) and the upper level Silk Road pattern (SRP)-like geopotential height anomalies. Along the north flank of the anomalous cyclonic circulation, easterly wind anomalies weaken climatological winds and prevent further movement of southwest moisture transport, leading to the enhancement of moisture convergence over HMs. Diagnosis shows that anomalous vertical motions are owing to the advection of anomalous temperature by basic zonal winds. The anomalous lower level cyclonic circulation over the northern SCS is related to La Niña-like sea surface cooling in the equatorial central and eastern Pacific. This cooling adjusts the Walker Circulation, causing positive precipitation anomalies near the SCS, which trigger the anomalous cyclonic circulation as a warm Rossby wave response. The distribution of upper level geopotential height anomalies over the mid-latitude Asian land resembles the SRP. Due to its barotropic structure, the SRP leads to warm and cold anomalies over the central Asia and the central China, respectively. The advection of anomalous temperature gradient by mean westerlies leads to anomalous ascending motions and more precipitation over HMs.

**KEY WORDS** the Hengduan Mountains; precipitation; vertical motions; SCS cyclone; central and eastern Pacific cooling; Silk Road pattern

Received 23 January 2017; Revised 15 September 2017; Accepted 24 September 2017

## 1. Introduction

The Hengduan Mountains (HMs), with an area of 500 000 km<sup>2</sup>, are located in the southeast of the Tibetan Plateau (TP), with the YunGui plateau and Bayan Har Mountains to their south and north sides, respectively (Li *et al.*, 2011; Zhang *et al.*, 2014a). HMs have the world's largest elevation drop from about 4800 m at the TP to about 600 m at the Sichuan basin, as shown in Figure 1. Weather and topography change greatly with location and altitude, corresponding with large differences in the distribution of biology communities, hydrologic features, and water resource. These complicated conditions play a crucial role in the local ecology, which shows the world's most important hot spots of biodiversity, containing more than 9000 species of plants, especially rich in endemic species and genera (Nie *et al.*, 2002).

Mountains and rivers exist alternately, with the Minshan Mountain, Minjiang River, Qinglai Mountain, Dadu River, Daxue Mountain, Yabi River, Shaluli Mountain, Jinsha River, Yunling Mountain, Lancang River, Nu Mountain, Nu River, Gaoligong Mountain from east to west, making the stereo-physiognomy with high mountains and deep valleys (Figure 1). Besides, several major rivers in Asia originate from this region, including the Yangtze River, the Yellow River, the Lancang River, and the Nu River. Mekong River and Salween River are the stretches of the Lancang River and the Nu River in China, respectively (Qin *et al.*, 2010). HMs region is one of the predominant boreal summer rainfall regions in the world. Precipitation variation over HMs has a great influence on glaciers, surface runoffs, and river discharge (Dong *et al.*, 2016). Moreover, HMs are located in the upstream of these rivers, and precipitation variation is important to both local and remote areas. Therefore, it is meaningful to investigate precipitation variability over HMs.

The climate over HMs is complicated, and controlled by both the South and East Asian summer monsoon (Zhu *et al.*, 2013; Zhang *et al.*, 2014a). There exists positive

\* Correspondence to: G. Huang, Institute of Atmospheric Physics, Chinese Academy of Sciences, P. O. Box 9804, Beijing 100029, China. E-mail: hg@mail.iap.ac.cn

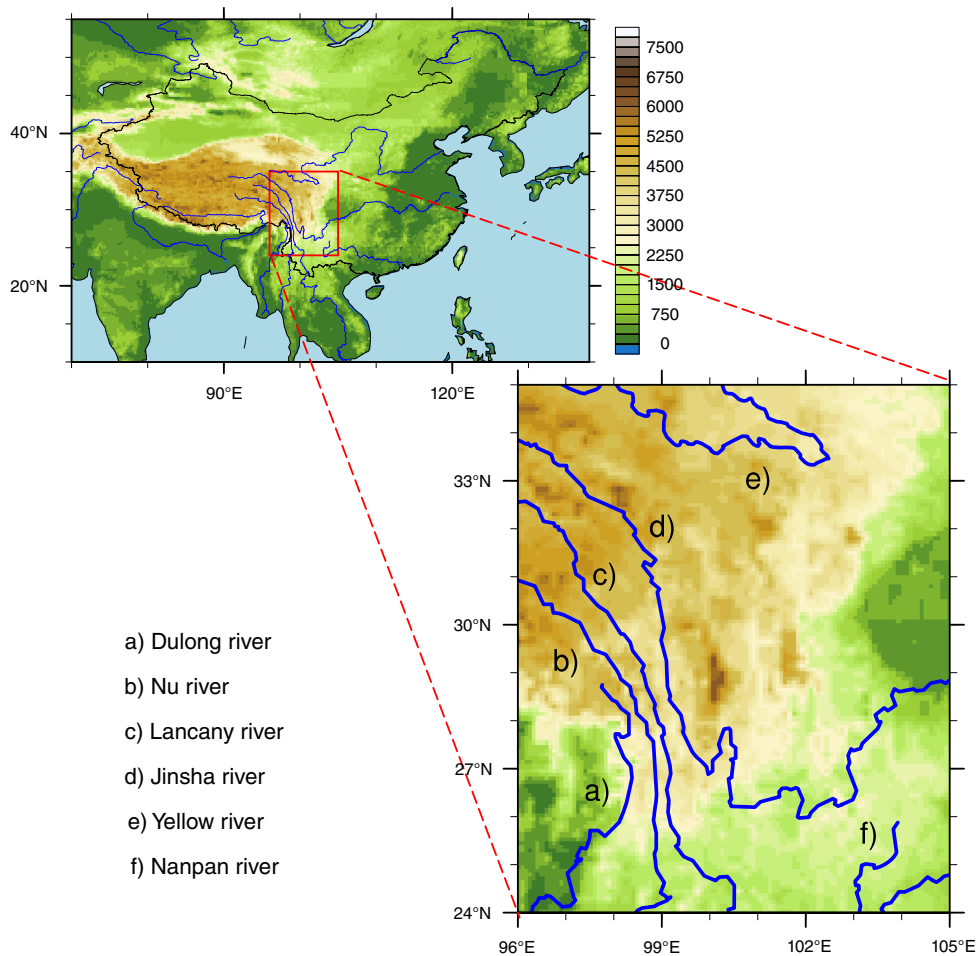


Figure 1. Topographic distribution over the South Asia and East Asia and main rivers over the HMs region. The box represents the HMs region ( $24^{\circ}40' - 34^{\circ}00'N$ ,  $96^{\circ}20' - 104^{\circ}30'E$ ). [Colour figure can be viewed at [wileyonlinelibrary.com](http://wileyonlinelibrary.com)].

correlation between the precipitation anomalies of HMs and East Asian Summer Monsoon Index (Zhang *et al.*, 2015). Sometimes, this area is suffered from drought due to the variation of the South Asian monsoon (Zhu *et al.*, 2016). Moreover, anomalous tropical sea-surface temperature (SST) is an important factor affecting the Asian monsoon, and anomalous atmospheric circulation over the northwest Pacific (NWP) plays an important role in bridging the connection from tropical SST anomalies to the East Asian climate (Zhang *et al.*, 1996; Chang *et al.*, 2000; Wang *et al.*, 2000; Wu *et al.*, 2003; Yang *et al.*, 2007; Xie *et al.*, 2009; Wang and Wu, 2012; Chen *et al.*, 2016; Tao *et al.*, 2016). Besides, processes at middle and high latitudes also affect the precipitation anomalies near HMs. Liu and Yin (2001) found that the seesaw structure of interannual summertime precipitation variation between the southern and northern parts of eastern TP is closely related to the North Atlantic Oscillation induced circulation change. Wu (2002) identified a dominant pattern for the interannual variation of upper-level winds over mid-latitude Asia in boreal summer: two anomalous anticyclones over the west Asia and mid-latitude East Asia and a cyclonic between the two large anticyclones. Lu *et al.* (2002) found a similar teleconnection pattern, and it

was named as the Silk Road pattern (SRP) later (Enomoto *et al.*, 2003). It forms as a result of the propagation of quasi-stationary Rossby waves along the Asian jet and has a wavelength of about  $60^{\circ}$  in the zonal direction (Lu *et al.*, 2002; Enomoto *et al.*, 2003; Sato and Takahashi, 2003; Kosaka *et al.*, 2009, 2012). SRP is viewed as a part of the circumglobal teleconnection (CGT) pattern that extends zonally through the whole hemisphere (Ding and Wang, 2005; Yasui and Watanabe, 2010; Chen and Huang, 2012; Lin, 2014) and can influence climate over a broad area, including precipitation and temperature over TP and East Asia (Liu and Yin, 2001; Wu, 2002; Bothe *et al.*, 2010, 2011; Gao *et al.*, 2013). Gao *et al.* (2013) studied the variation of summer precipitation over the southeastern part of TP, and emphasized the importance of Atlantic SST anomalies by triggering CGT-like zonal wave pattern.

At present, the researches about the HMs are rare, and most of them focus on the analysis of main meteorological elements. Both annual and seasonal means of daily maximum, minimum, and mean temperature exist significant warming trends, while the increasing trend is insignificant for annual precipitation (Ban *et al.*, 2006; Ma *et al.*, 2006; Qin *et al.*, 2010; Li *et al.*, 2011). By calculating 12 indices of extreme precipitation, Zhang *et al.*, (2014a) found that

only three indices have significant trends. The total precipitation and extreme precipitation trends both decrease from southwest to northeast over the HMs (Li *et al.*, 2011; Zhang *et al.*, 2014a). Besides, the seasonal evolution of precipitation has a unique characteristic, which is highly linked to the topographic factors and wind fields (Xiao *et al.*, 2013). Until now, there is still no systematic study about precipitation variability over the HMs region. Thus, the purpose of present study is to investigate the interannual variability of precipitation over HMs by using the high resolution datasets, which are better to investigate the characteristic of precipitation variation, its related circulation anomalies, main impact factors, and possible mechanism over the complex terrain area. The rest of paper is organized as follows. Section 2 introduces data and methods. Section 3 describes the spatiotemporal characteristics of HMs precipitation in rainy season and the associated atmospheric circulation. Possible mechanism is explored in Section 4. Section 5 gives the conclusion and discussion.

## 2. Data and methods

### 2.1. Data

The observed daily precipitation data analysed in this study is from the National Climatic Center of the China Meteorological Administration with 2472 high density national meteorological stations during 1979–2014. Following previous studies (Li *et al.*, 2011; Zhang *et al.*, 2014a), HM region is defined as a rectangular domain of 24°40′–34°00′N and 96°20′–104°30′E, as shown in Figure 1. Stations with more than 7 days' missing data are removed, and the rest of 151 stations over HMs are analysed. The spatial distribution of 151 weather observation sites is shown in Figure 2(a). HMs have the great elevation drop from northwest to southeast, and stations are scattered in highland while gathered in lowland. The numbers of stations at different altitude, from near 600 to 4800 m, are presented in Figure 2(b). Most stations are located below 3000 m and the number of stations reaches its peak around 2000 m (Figure 2(b)). Besides, the observed daily precipitation data from 839 standard meteorological stations are also used to further verify results, and 50 stations over HMs without missing value are selected. The global precipitation dataset used in this study is the monthly mean Climate Prediction Center Merged Analysis of Precipitation (CMAP) on a 2.5° × 2.5° grid (Xie and Arkin, 1997), which is available starting from 1979.

Monthly atmospheric variables used in the present study are obtained from the ERA-Interim (Dee *et al.*, 2011). It is a newly reanalysis product provided by the European Centre for Medium-Range Weather Forecasts (ECMWF) and has a 0.5° × 0.5° horizontal resolution. The variables include horizontal winds, vertical velocity, specific humidity, air temperature, and geopotential height. The monthly SST data are obtained from NOAA Extended Reconstructed Sea Surface Temperature (ERSST) V4 version on a 2° × 2° grid (Huang *et al.*, 2015). Topographic

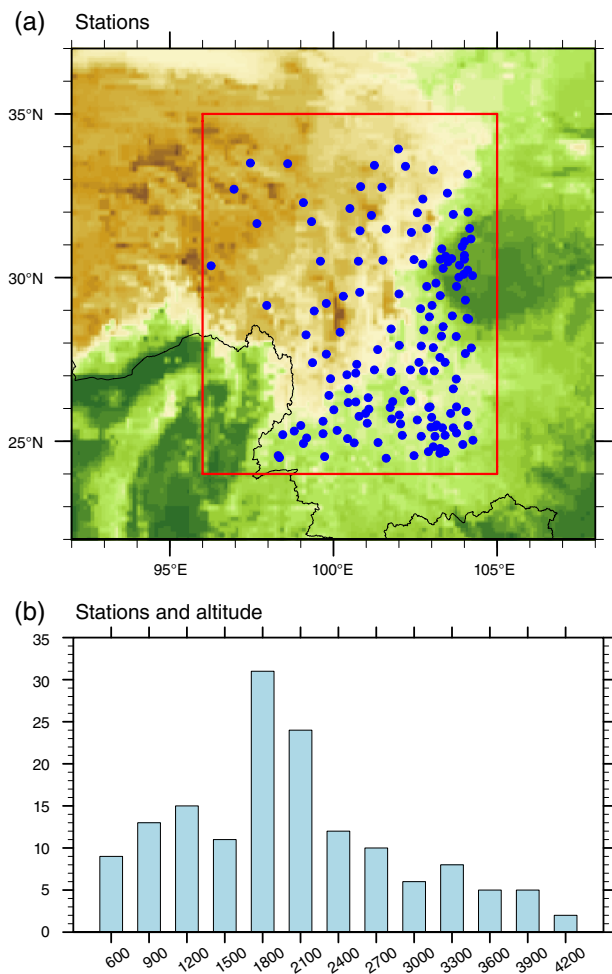


Figure 2. (a) Location of 151 stations over HMs, and (b) numbers of stations at different altitudes. [Colour figure can be viewed at [wileyonlinelibrary.com](http://wileyonlinelibrary.com)].

dataset used in this study is from NOAA (<http://www.ngdc.noaa.gov/mgg/topo/topo.html>). It is generated from a digital data base of land and sea-floor elevations on a 5° × 5° grid. Note that the present analysis is restricted to the period from 1979 to 2014.

### 2.2. Methods

Moisture diagnosis is used in the present study. According to Trenberth (1991), vertically integrated water vapour flux can be expressed as:

$$Q_u = \frac{1}{g} \int_{p_s}^{p_t} q u dp \quad (1)$$

$$Q_v = \frac{1}{g} \int_{p_s}^{p_t} q v dp \quad (2)$$

Here  $p$ ,  $q$ ,  $u$ ,  $v$ , and  $g$  represent the pressure, specific humidity, zonal wind, meridional wind, and the acceleration due to gravity, respectively.  $p_s$  is the surface pressure and the pressure of top layer  $p_t$  is equal to 100 hPa in this study as the water vapour flux above 100 hPa is negligible.

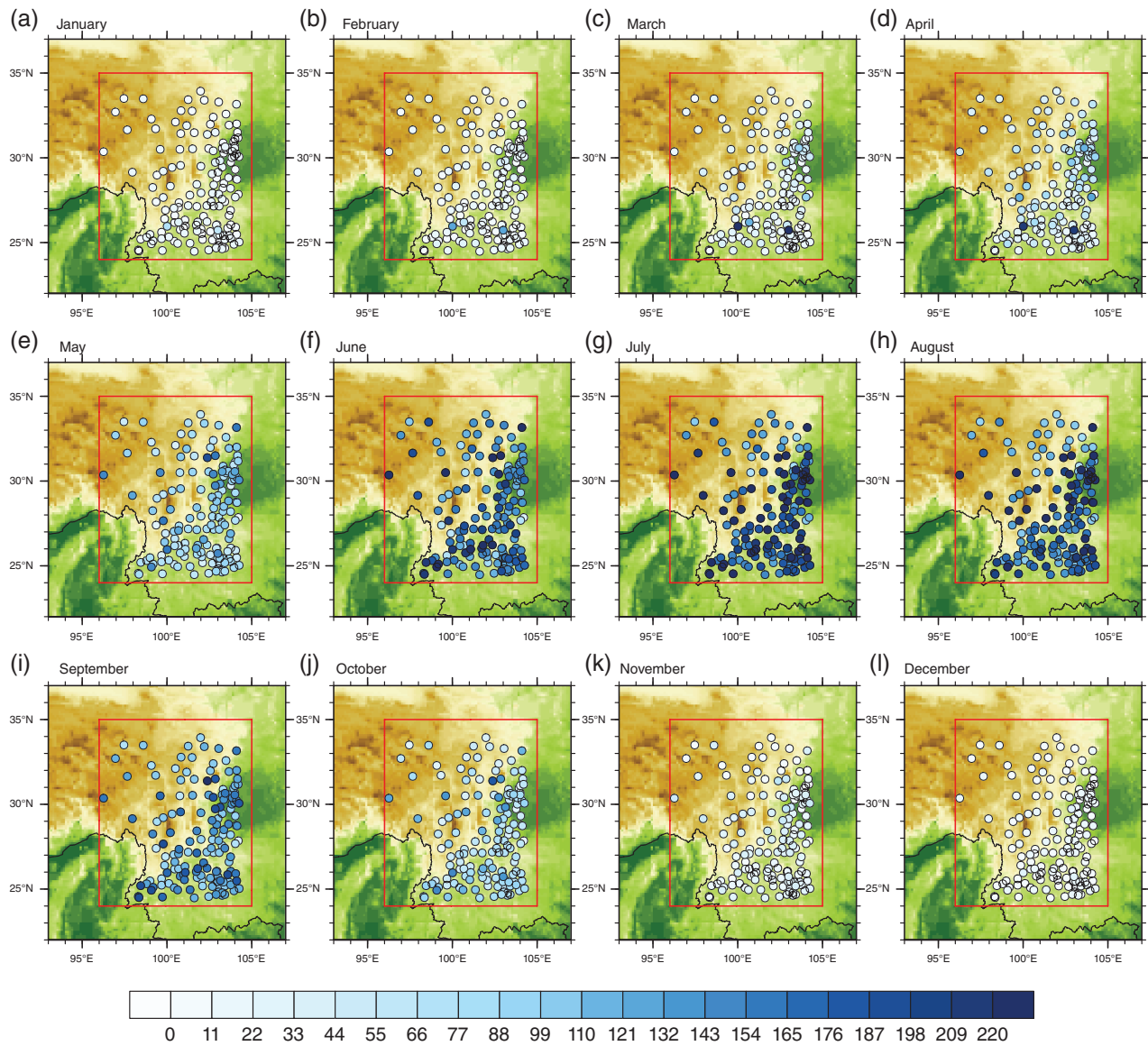


Figure 3. Climatological monthly mean precipitation (mm) at 151 stations over HMs from January to December. [Colour figure can be viewed at [wileyonlinelibrary.com](http://wileyonlinelibrary.com)].

The divergence of water vapour flux can be divided into two parts: the wind divergence term and the moisture advection term (Huang *et al.*, 1998; Qu *et al.*, 2015):

$$\langle -\nabla \cdot (qV)' \rangle = \langle -(q\nabla \cdot V)' \rangle + \langle -(V \cdot \nabla q)' \rangle \quad (3)$$

The variable with prime means the departure from climatological mean state.  $q$  and  $V$  represent specific humidity and horizontal wind. The value in angle bracket means a mass integration from the surface to 100 hPa, that is:

$$\langle X \rangle = -\frac{1}{g} \int_{\text{surface}}^{100 \text{ hPa}} X dp$$

Quasi-geostrophic omega equation is used to diagnose the formation mechanism of the vertical motions. The quasi-geostrophic equation is taken as:

$$\underbrace{\left( \sigma \nabla^2 + f_0^2 \frac{\partial^2}{\partial p^2} \right)}_A \omega = \underbrace{f_0 \frac{\partial}{\partial p} \left[ \vec{V}_g \cdot \nabla (\zeta_g + f) \right]}_B + \underbrace{\frac{R}{p} \nabla^2 \left[ \vec{V}_g \cdot \nabla T \right]}_C - \underbrace{\frac{R}{c_p p} \nabla^2 \frac{dQ}{dt}}_D \quad (4)$$

Where all operators and variables are of conventional usage in meteorology. The term on the left-hand side of Equation (4) is the Laplacian of omega and approximately equivalent to omega multiplied by a negative coefficient (Term A). Terms on the right-hand side are the vertical difference of geostrophic absolute vorticity advection (Term B), the Laplacian of geostrophic temperature advection (Term C), and the Laplacian of diabatic heating (Term D), respectively. Term D has the same physical meaning with

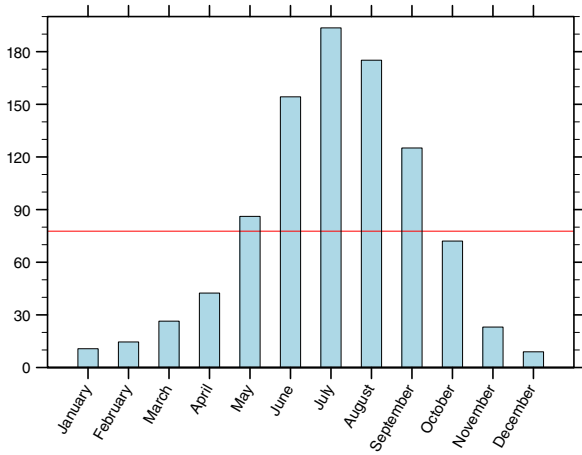


Figure 4. Climatological monthly mean precipitation (mm) averaged over HMs. The line represents the annual mean. [Colour figure can be viewed at wileyonlinelibrary.com].

Term C because precipitation can release condensation, which will reinforce ascending motions and then produce more precipitation in turn. Thus, in the following, we diagnose Term B and Term C, by separating each variable into a time-averaged basic state and its departure (Peixóto and Oort, 1984; Wei *et al.*, 2014; Zhao *et al.*, 2015). Then Term B and Term C in Equation (4) can be written as:

$$\begin{aligned}
 f_0 \frac{\partial}{\partial p} [\bar{v}_g \cdot \nabla (\zeta_g + f)] &= f_0 \frac{\partial}{\partial p} \left[ (\bar{v}_g + \bar{v}'_g) \cdot \nabla (\bar{\zeta}_g + \zeta'_g) + \frac{\partial f}{\partial y} \right] \\
 &= f_0 \frac{\partial}{\partial p} \left[ \left( \bar{u}_g \frac{\partial \bar{\zeta}_g}{\partial x} + \bar{u}'_g \frac{\partial \bar{\zeta}_g}{\partial x} + \bar{u}_g \frac{\partial \zeta'_g}{\partial x} + \bar{u}'_g \frac{\partial \zeta'_g}{\partial x} + \bar{v}_g \frac{\partial \bar{\zeta}_g}{\partial y} + \bar{v}'_g \frac{\partial \bar{\zeta}_g}{\partial y} \right. \right. \\
 &\quad \left. \left. + \bar{v}_g \frac{\partial \zeta'_g}{\partial y} + \bar{v}'_g \frac{\partial \zeta'_g}{\partial y} \right) \right] + \left( \bar{v}_g \frac{\partial f}{\partial y} + \bar{v}'_g \frac{\partial f}{\partial y} \right) \quad (4a)
 \end{aligned}$$

$$\begin{aligned}
 \frac{R}{p} \nabla^2 [\bar{v}_g \cdot \nabla T] &= \frac{R}{p} \nabla^2 \left[ (\bar{v}_g + \bar{v}'_g) \cdot \nabla (\bar{T} + T') \right] \\
 &= \frac{R}{p} \nabla^2 \left( \bar{u}_g \frac{\partial \bar{T}}{\partial x} + \bar{u}'_g \frac{\partial \bar{T}}{\partial x} + \bar{u}_g \frac{\partial T'}{\partial x} + \bar{u}'_g \frac{\partial T'}{\partial x} + \bar{v}_g \frac{\partial \bar{T}}{\partial y} + \bar{v}'_g \frac{\partial \bar{T}}{\partial y} + \bar{v}_g \frac{\partial T'}{\partial y} + \bar{v}'_g \frac{\partial T'}{\partial y} \right) \quad (4b)
 \end{aligned}$$

The variables with bar and prime are their basic state and perturbation, respectively. Considering that the basic state variables themselves satisfy the equation, the omega equation of perturbation can be written as:

$$\begin{aligned}
 \underbrace{(\sigma \nabla^2 + f_0^2 \frac{\partial^2}{\partial p^2}) \omega'}_A &= f_0 \frac{\partial}{\partial p} \left( \underbrace{u'_g \frac{\partial \bar{\zeta}_g}{\partial x}}_{B1} + \underbrace{u_g \frac{\partial \zeta'_g}{\partial x}}_{B2} + \underbrace{u'_g \frac{\partial \zeta'_g}{\partial x}}_{B3} + \underbrace{v'_g \frac{\partial \bar{\zeta}_g}{\partial y}}_{B4} \right. \\
 &\quad \left. + \underbrace{v_g \frac{\partial \zeta'_g}{\partial y}}_{B5} + \underbrace{v'_g \frac{\partial \zeta'_g}{\partial y}}_{B6} + \underbrace{v'_g \frac{\partial f}{\partial y}}_{B7} \right) \\
 &+ \frac{R}{p} \nabla^2 \left( \underbrace{u'_g \frac{\partial \bar{T}}{\partial x}}_{C1} + \underbrace{u_g \frac{\partial T'}{\partial x}}_{C2} + \underbrace{u'_g \frac{\partial T'}{\partial x}}_{C3} + \underbrace{v'_g \frac{\partial \bar{T}}{\partial y}}_{C4} + \underbrace{v_g \frac{\partial T'}{\partial y}}_{C5} + \underbrace{v'_g \frac{\partial T'}{\partial y}}_{C6} \right) \quad (5)
 \end{aligned}$$

$\sigma, f_0, p, \omega, \zeta_g, u_g, v_g,$  and  $T$  represent specific volume, the vertical component of planetary vorticity, pressure, vertical velocity, quasi-geostrophic vortex, zonal wind, meridional wind, and temperature, respectively.

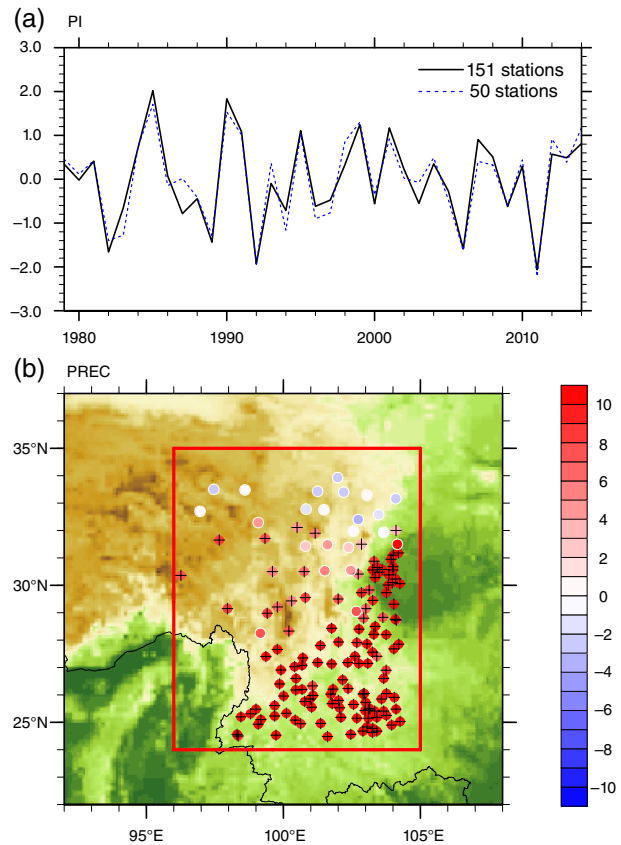


Figure 5. (a) Normalized precipitation anomalies averaged at 151 stations (solid line) and 51 stations (dashed line) over HMs during rainy season. (b) Regression of precipitation (mm) with respect to PI at 151 stations over HMs during rainy season. The cross marks indicate that the significant level reaches 90%. [Colour figure can be viewed at wileyonlinelibrary.com].

Besides, to extract interannual signals, we perform a 9-year running average to reduce decadal variability. Regression and correlation analysis are used, and the significance level is estimated based on the standard two-tailed Student’s *t*-test.

### 3. The spatiotemporal characteristics of HMs precipitation and associated atmospheric circulation

#### 3.1. Climatological setting

Figure 3 shows the spatial distributions of climatological monthly precipitation during 1979–2014. Precipitation over HMs has significant month-to-month changes. The climatological monthly precipitations from November to April are under 30 mm in most stations, which account for 88, 100, 99, 96, 93, and 78% stations over the HMs, respectively. While significant increase exists from May to September, reaching its peak and exceeding 200 mm in 72% stations over the HMs during July (Figure 3). Besides, there is more precipitation in the southern and eastern part than the northern part of HMs region with altitude exceeding 2 km. The average of monthly precipitation at all stations over HMs is above the annual mean from May to September, while the sum of rest months is below 20%

of annual total precipitation (Figure 4). Thus, we define the rainy season over HMs as the period from May to September, which is consistent with previous studies (Gao *et al.*, 2013; Xiao *et al.*, 2013).

### 3.2. Interannual variability of precipitation

The normalized precipitation anomaly averaged at all stations over HMs during rainy season is defined as the precipitation index (PI) in the present study. As shown in Figure 5(a), the PI exists significant interannual variability, and the years 1985, 1990, 1991, 1995, 1999, and 2001 show the significant excessive rainfall, and 1982, 1989, 1992, 2006, and 2011 are low rainfall years. The results calculated by using 50 stations match well with that using the 151 stations, with a correlation coefficient of 0.97. Hereafter, we only present results based on the PI of 151 stations. Figure 5(b) shows the regression of precipitation with respect to PI over HMs during rainy season. Precipitation shows a consistent interannual variation in 92% stations over the HMs, and the magnitude displays decreasing tendency from southeast to northwest corresponding to the increase of altitude with  $-8.6 \text{ mm km}^{-1}$ . The largest precipitation anomalies exist over the southeastern part of HMs and the western Sichuan Basin where the values are larger than  $10 \text{ mm month}^{-1}$ . The signal over the northern HMs, especially north of  $33^\circ\text{N}$ , is weak even without reaching the 90% significance level. Note that removing these stations over the northern HMs or not removing does not alter the main conclusions.

### 3.3. Associated atmospheric circulation anomalies

Figure 6 presents the regression of 700 hPa horizontal wind, 500 hPa vertical velocity, and 200 hPa geopotential height with respect to PI during rainy season. In the lower level, the HMs region is mainly controlled by an anomalous cyclonic circulation over the northern South China Sea (SCS), and there are significant easterly wind anomalies at its north flank (Figure 6(a)). Due to the dynamical influence of topography, the easterly winds bifurcate on the east side of HMs, turning into northeasterly winds south of  $31^\circ\text{N}$  and weak southerly winds north of  $31^\circ\text{N}$ . Besides, there are anomalous southwesterly winds from the Bay of Bengal via the south boundary of HMs, and the southwesterlies turn southward along the topography of HMs. Although that there exist anomalous descending motions over the northwestern HMs, most south part of HMs are controlled by anomalous ascending motions (Figure 6(b)). A notable low pressure center at the upper level is located over the southern China, and there are two anomalous high pressure on its west and northeast side, respectively (Figure 6(c)). Thus, the anomalous low pressure over the southern China displays a barotropic vertical structure. Abundant moisture transport and strong ascending motions are the two necessary conditions for precipitation. The relationship between atmospheric circulation anomalies and these two factors over the HMs region will be further explored in the next section.

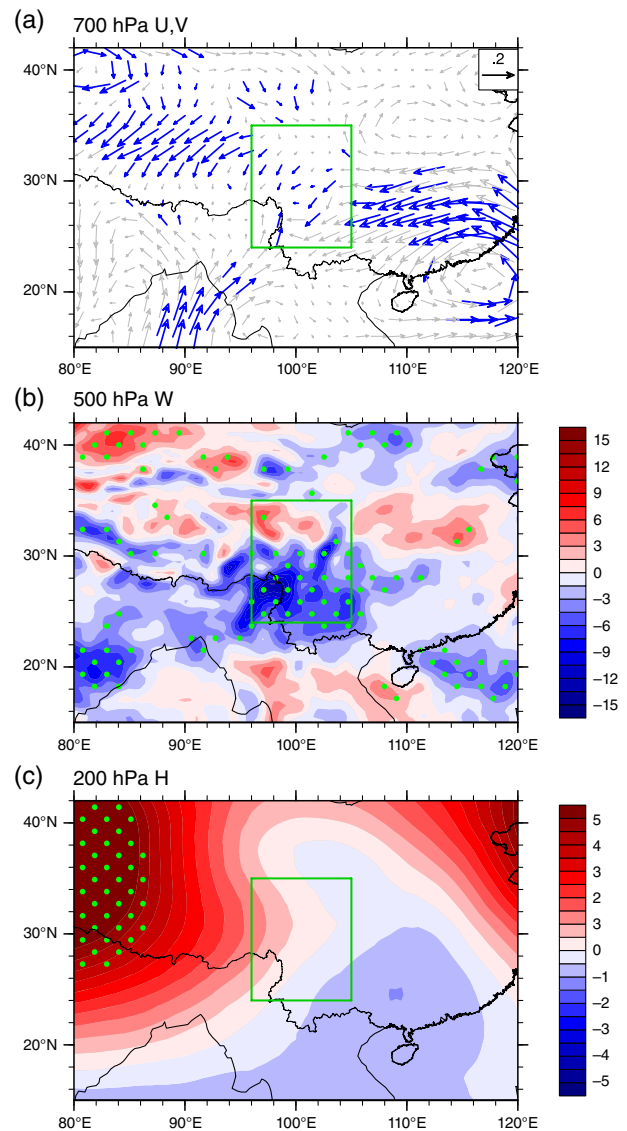


Figure 6. Regression of (a) 700 hPa horizontal wind ( $\text{m s}^{-1}$ ), (b) 500 hPa vertical velocity ( $10^{-3} \text{ Pa s}^{-1}$ ), and (c) 200 hPa geopotential height (gpm) with respect to PI during rainy season. Thick vectors and dots indicate that the significant level reaches 90%. [Colour figure can be viewed at [wileyonlinelibrary.com](http://wileyonlinelibrary.com)].

## 4. Possible mechanism

### 4.1. Diagnostic analysis

#### 4.1.1. Moisture transport

Water vapour flux divergence is an important indicator for the variation of monsoon precipitation. Previous studies have concluded that the moisture flux divergence in the monsoon region is consistent with the distribution of precipitation (Chen and Tzeng, 1990; Huang *et al.*, 1998). Figure 7 presents the regression and climatology of column-integrated moisture flux and its divergence  $\langle -\nabla \cdot (qV) \rangle$ . Most of the HMs region is under the influence of anomalous convergence except for the northern part (Figure 7(a)). The pattern of moisture flux anomalies resembles that of 700 hPa wind anomalies (Figure 6(a)). The climatology state shows the major

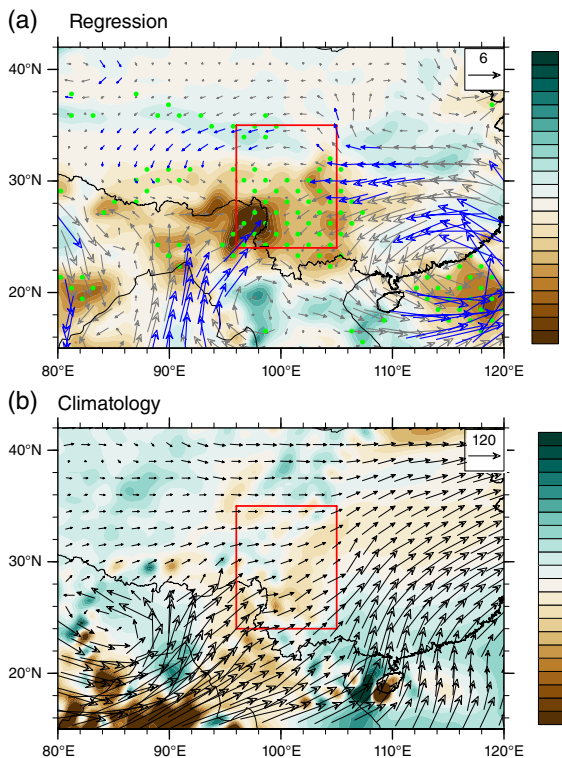


Figure 7. (a) Regression of vertically integrated water vapour flux (vector;  $\text{kg s}^{-1} \text{m}^{-1}$ ) and moisture divergence (shaded;  $10^{-5} \text{kg s}^{-1} \text{m}^{-1}$ ) with respect to PI during rainy season. (b) Climatology of vertically integrated water vapour flux (vector;  $\text{kg s}^{-1} \text{m}^{-1}$ ) and moisture divergence (shaded;  $10^{-5} \text{kg s}^{-1} \text{m}^{-1}$ ) during rainy season. Thick vectors and dots indicate that the significant level reaches 90%. [Colour figure can be viewed at [wileyonlinelibrary.com](http://wileyonlinelibrary.com)].

contribution of South Asian summer monsoon, and southwest winds are blocked by HMs (Figure 7(b)). However, there are two anomalous cyclonic systems affecting inter-annual variation of moisture budget over HMs. One is the cyclonic wind anomalies over the Bay of Bengal, which reinforce the southwesterly winds of South Asian summer monsoon and bring more moisture from the Indian Ocean. Another is the anomalous cyclone over the NWP. The easterly wind anomalies at its north flank weaken East Asian summer monsoon, and prevent the southwest moisture transport from further moving. Thus, these two cyclones enhance the moisture convergence over HMs.

To compare the relative importance of the two anomalous cyclones, we estimate the moisture flux anomalies across each boundary over HMs (Table 1). The most significant moisture flux anomalies are  $49.3 \times 10^3 \text{kg s}^{-1}$  via the eastern boundary. The moisture inputs via the western and southern boundary make a small contribution, and the sum of them is  $12.7 \times 10^3 \text{kg s}^{-1}$ . Although the southwest winds are slightly enhanced, the easterly wind anomalies block further forward movement of southwest moisture transport, mainly leading to the enhancement of moisture convergence over HMs. Thus, the precipitation over HMs is mainly affected by the anomalous easterlies, and the related northern SCS cyclone seems to be the key system.

We also analysed the relative contribution of wind and moisture anomalies.  $\langle -\nabla \cdot (qV) \rangle'$  is decomposed

Table 1. Boundary atmospheric fluxes via four boundaries, net zonal and meridional boundary atmospheric flux ( $10^3 \text{kg s}^{-1}$ ).

South	North	Net meridional	West	East	Net zonal
5.5	1.0	4.5	7.2	-49.3	56.5

into circulation term  $\langle -(q\nabla \cdot V) \rangle'$  and moisture term  $\langle -(V \cdot \nabla q) \rangle'$ . The detailed information of the moisture budget equation (Equation (3)) is introduced in Section 2.2. The circulation term  $\langle -(q\nabla \cdot V) \rangle'$ , which accounts for 93% of  $\langle -\nabla \cdot (qV) \rangle'$ , plays a more important role than moisture term  $\langle -(V \cdot \nabla q) \rangle'$  (figures not shown).

#### 4.1.2. Vertical motions

Because the vertical motion has a close relationship with precipitation, the quasi-geostrophic omega equation (Equation (5)) is used to diagnose the formation mechanism of vertical motions. Figure 8(a) presents the vertical profile of vertical velocity anomalies averaged over the southern part of HMs, where exists significant anomalous ascending motions (Figure 6(b)). The maximum vertical velocity is at 450 hPa and its regression pattern resembles the pattern at 500 hPa (figure not shown). The level 450 hPa can be regarded as a non-divergence level, which is suitable to diagnose the factors for the vertical motions.

Furthermore, the 450 hPa vertical velocity anomalies over HMs are decomposed into 13 terms (Equation (5)) to find out the main contributors. Figure 8(b) shows the results, and the terms on the right hand side of Equation (5) are denoted by B1–B7 and C1–C6. From the figure, the C2 term is dominant in the anomalous ascending motions over HMs, related to the advection of anomalous temperature by basic zonal winds. Note that the B2 term, which is the advection of anomalous relative vorticity by basic zonal winds, contributes to descending motions, but it counteracts the other B terms.

The contribution of the C2 term is illustrated in Figure 9. As shown in Figure 9(a), most of the HMs region appears the anomalous warm advection, which is consistent with the ascending motions in Figure 6(b). Because of the westward increase of temperature anomalies, basic westerly winds prevailing over the north of  $27^\circ\text{N}$  cause warm advection over HMs (Figure 9(b)). Furthermore, the warm advection leads to ascending motions. Note that the temperature anomalies correspond well with the barotropic structure of circulation anomalies (Figures 6(a), 6(c), and 9(b)). Thus, the diagnostic results of moisture transport and vertical motions both emphasize the importance of circulation anomalies. In the next subsections, the formation mechanism of circulation anomalies is further explored.

#### 4.2. SST anomalies

Previous studies have revealed that circulation anomalies located near the NWP are sensitive to the tropical ocean status. Local SST anomalies (Wang *et al.*, 2000; Wang and Zhang, 2002), or the remote ocean status, as the tropical Indian Ocean SST anomalies (Yang *et al.*, 2007, 2010;

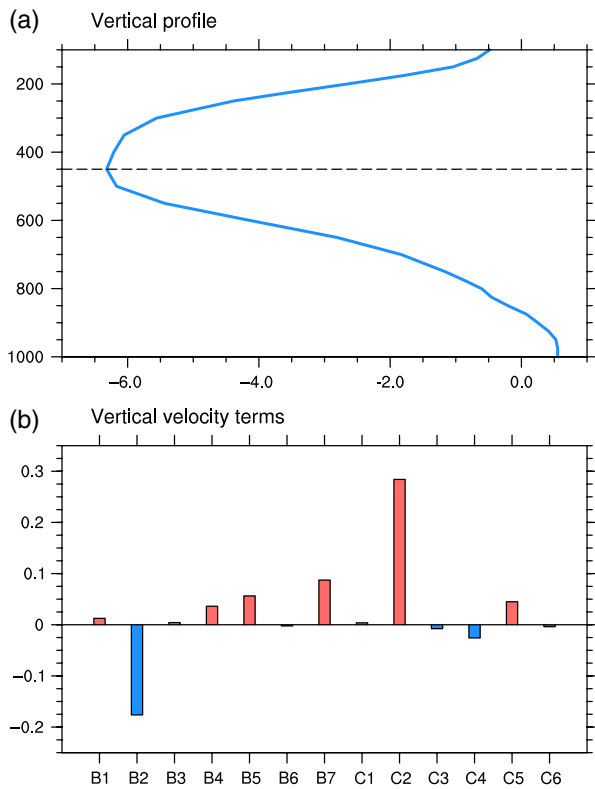


Figure 8. (a) Vertical profile of the regressed vertical velocity anomalies ( $10^{-3} \text{ Pa s}^{-1}$ ) averaged over HMs. (b) Seven terms of  $f_0 \frac{\partial}{\partial p} [\vec{V}_g \cdot \nabla (\zeta_g + f)]$  denoted by B1–B7 and six terms of  $\frac{R}{p} \nabla^2 [\vec{V}_g \cdot \nabla T]$  denoted by C1–C6 averaged over HMs at 450 hPa ( $10^{-19} \text{ m s}^{-1} \text{ kg}^{-1}$ ). [Colour figure can be viewed at [wileyonlinelibrary.com](http://wileyonlinelibrary.com)].

Wu *et al.*, 2009; Xie *et al.*, 2009, 2016; Xie and Zhou, 2017), equatorial central and eastern Pacific (CEP) SST anomalies (Wang *et al.*, 2013; Xiang *et al.*, 2013; Chen *et al.*, 2016; Chowdary *et al.*, 2016a, 2016b; Tao *et al.*, 2016), all contribute to the development and maintenance of anomalous circulation.

Figure 10 presents the regression of 700 hPa wind, 500 hPa vertical velocity, SST, and precipitation with respect to PI during rainy season. There exhibits a dipole structure of SST anomalies over the Pacific. It is a La Niña-like pattern, with cooling over the equatorial CEP, and warming over the western Pacific and much of the northern and southern Pacific (Figure 10(b)). The CEP index (CEPI) is defined as the SST anomalies averaged over the CEP ( $5^\circ\text{S}–5^\circ\text{N}$ ,  $130^\circ–100^\circ\text{W}$ ), and the correlation coefficient between the PI and CEPI is 0.33 reaching the 95% confidence level. The cooling induces lower (upper) level divergence (convergence) over the CEP and then the descending motions and negative precipitation anomalies (Figures 10(a), 10(c), and 11). Furthermore, the Walker Circulation is adjusted, and there are ascending motions and positive precipitation anomalies with lower (upper) level convergence (divergence) over the SCS and the Maritime Continent. As a result, the northern SCS cyclonic anomalies are triggered as a warm Rossby wave response to the positive precipitation anomalies

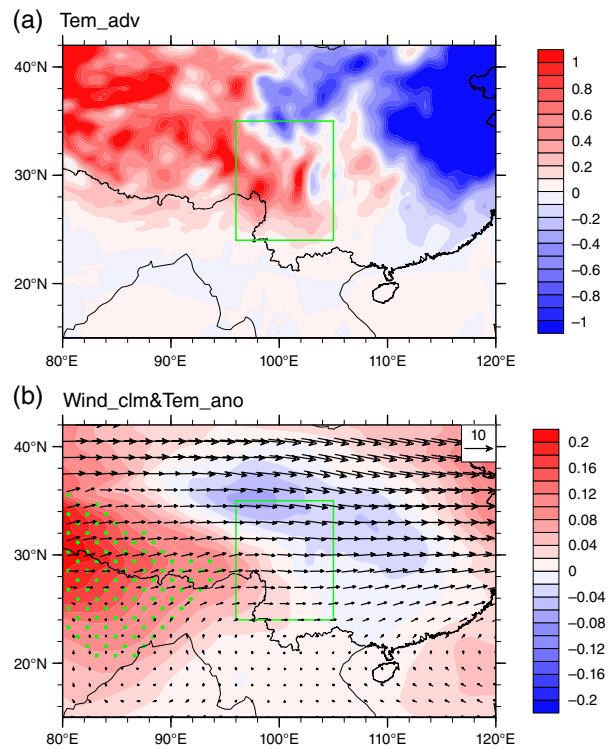


Figure 9. (a) The advection of anomalous temperature by basic zonal winds ( $-\bar{u}_g \frac{\partial T'}{\partial x}$ ,  $10^{-6} \text{ K s}^{-1}$ ). (b) Regression of temperature with respect to PI (shaded, K) and climatological horizontal wind (vector,  $\text{m s}^{-1}$ ) at 450 hPa during rainy season. Dots indicate that the significant level reaches 90%. [Colour figure can be viewed at [wileyonlinelibrary.com](http://wileyonlinelibrary.com)].

(Figure 10(a)). Tao *et al.* (2016) suggested similar processes by which the CEP cooling could influence the circulation anomalies located near the NWP. The cooling causes the wet anomalies over the Maritime Continent and NWP through large-scale circulation adjustment, and then the wet anomalies further trigger anomalous lower level cyclonic circulation over the NWP. Note that the negative rainfall anomalies shift more westward than the negative SST anomalies. Due to the normally dry condition over the eastern cold tongue region, the large negative SST anomalies can hardly further suppress convection and cause the weak rainfall response.

### 4.3. Silk road pattern

Figure 12(a) presents the PI regressed 200 hPa geopotential height anomalies during rainy season. A zonal teleconnection emerges from the North Atlantic Ocean to East Asia. There are five prominent ‘centres of action’, presenting ‘+’ and ‘-’ geopotential height anomalies alternately. The geopotential height anomalies over the Greenland-North Atlantic Ocean, the west-central Asia, and the northeast Asia are in phase with each other, as shown by the significant positive anomalies. In contrast, there are negative geopotential height anomalies over the European Russia and the central China. Note that the negative geopotential height anomalies over the central China are weak and insignificant. The whole pattern of geopotential height anomalies and wave activity fluxes seem

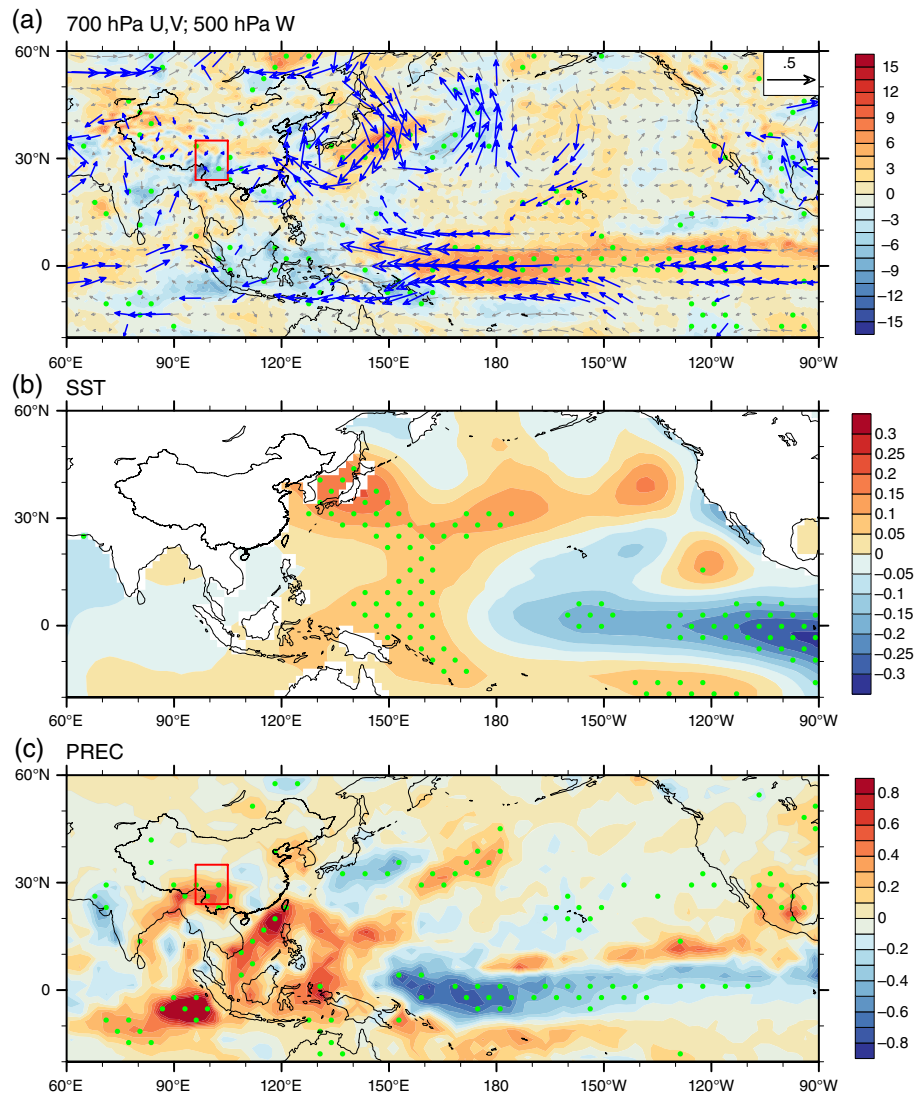


Figure 10. Regression of (a) 700 hPa horizontal wind ( $\text{m s}^{-1}$ ) and 500 hPa vertical velocity ( $10^{-3} \text{ Pa s}^{-1}$ ), (b) SST ( $^{\circ}\text{C}$ ), and (c) precipitation (mm) with respect to PI during rainy season. Thick vectors and dots indicate that the significant level reaches 90%. [Colour figure can be viewed at [wileyonlinelibrary.com](http://wileyonlinelibrary.com)].

to resemble that of SRP (or CGT) (Lu *et al.*, 2002; Wu, 2002; Ding and Wang, 2005; Bothe *et al.*, 2010; Gao *et al.*, 2013). The SRP is characterized by the stationary Rossby waves along the Asian jet (Lu *et al.*, 2002; Wu, 2002; Ding and Wang, 2005; Lin, 2014) that acts as a waveguide and confines the waves within it (Hoskins and Ambrizzi, 1993). Thus, the SRP can influence the climate over a broad area (Lu *et al.*, 2002; Wu, 2002; Huang *et al.*, 2011; Chen and Huang, 2012; Lin, 2014). Bothe *et al.* (2010) and Gao *et al.* (2013) have investigated that the SRP related wave trains emerge from the North Atlantic, and pass through the Mediterranean to Asia, resulting in the precipitation anomalies near the TP. Following the previous studies, an SRP index (SRPI) is defined as the first leading EOF mode of the 200 hPa meridional winds during rainy season in the domain of  $20^{\circ}$ – $60^{\circ}\text{N}$ ,  $0^{\circ}$ – $150^{\circ}\text{E}$  (Yasui and Watanabe, 2010; Chen and Huang, 2012; Hong and Lu, 2016). The correlation coefficient between the PI and SRPI is 0.48 reaching the 99% confidence level. The SRPI regressed

geopotential height pattern resembles Figure 12(a), which further suggests that the SRP could influence anomalous circulation over the HMs (Figure 12(b)).

Due to the barotropic structure of SRP, the geopotential height anomalies correspond well with the temperature anomalies, with the high pressure centres co-locating with warm centres, and vice versa (Figures 9(b) and 12(a)). There are positive and negative geopotential height anomalies over the central Asia and the central China, respectively, resulting in the gradient of temperature anomalies. As a result, the basic zonal flow causes the warm advection, which influences the anomalous ascending motions over the HMs.

Furthermore, for the CEP SST anomalies and SRP, how these two factors work together to influence the HMs rainfall, and what role does each of them play? Thus, all years for high and low HMs PI are classified into three groups according to the CEPI, SRPI, or both of them, as presented in Table 2. Only 2 years show that the CEP SST

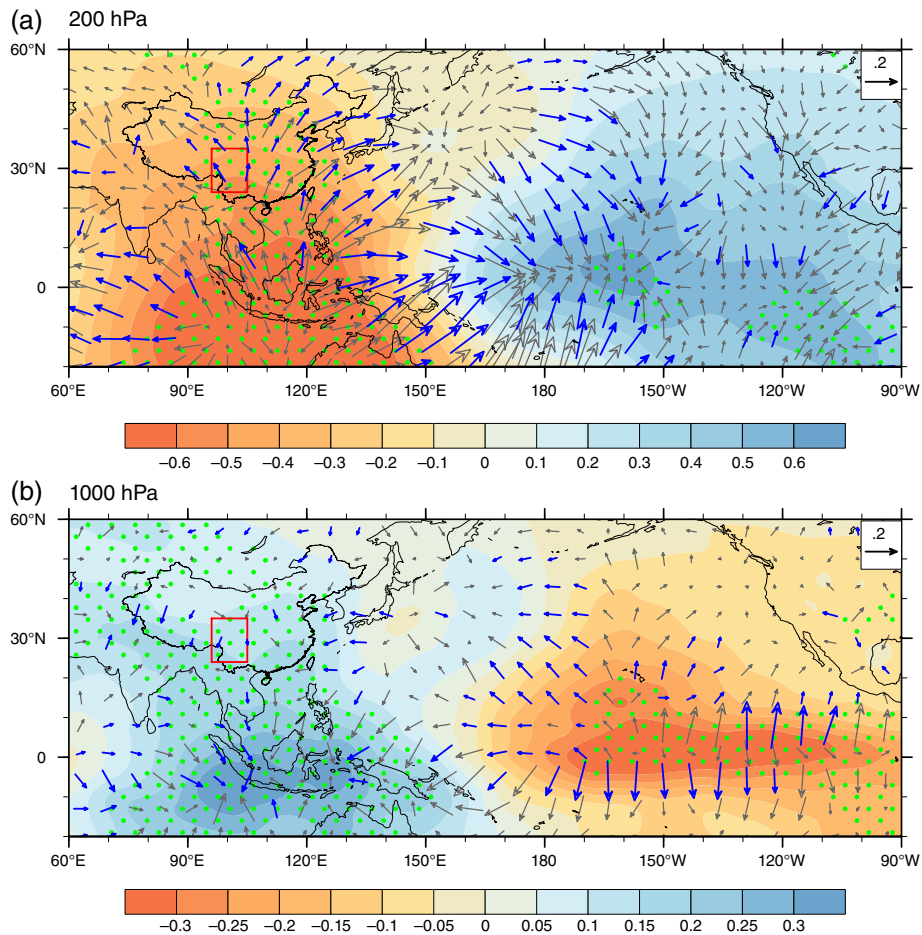


Figure 11. Regression of potential velocity (contour;  $10^5 \text{ m}^2 \text{ s}^{-1}$ ) and relevant divergent wind component (vector,  $\text{m s}^{-1}$ ) with respect to PI during rainy season at (a) 200 hPa and (b) 1000 hPa. Thick vectors and dots indicate that the significant level reaches 90%. [Colour figure can be viewed at [wileyonlinelibrary.com](http://wileyonlinelibrary.com)].

anomalies or SRP has a single impact on the positive HMs rainfall anomalies, and there are 10 years indicating these two factors work together and cause the rainfall anomalies. Thus, the combined effect of CEP SST anomalies and SRP has a crucial influence on HMs rainfall, rather than anyone of their single effect. Actually, these two factors reflect the different aspects of circulation anomalies. The CEP cooling plays a dominant role in influencing the SCS cyclone, which transports abundant moisture over the HMs, and the SRP is mainly related to the ascending motions.

**5. Conclusion and discussion**

In this paper, we have studied the interannual variation of precipitation over HMs during rainy season and its causes. Precipitation shows a consistent interannual variation over most of HMs region, with a decreasing tendency of magnitude from southeast to northwest following the increase of altitude. Corresponding to more precipitation over the HMs region, there are lower level cyclonic circulation anomalies over the northern SCS, and upper level SRP-like geopotential height anomalies. Besides, there are cyclonic wind anomalies over the Bay of Bengal, which slightly reinforce the southwesterly winds and transport more

moisture from the Indian Ocean. However, the precipitation over HMs is mainly affected by the anomalous easterly winds, which are at the north flank of anomalous cyclonic circulation. The easterly wind anomalies weaken climatology winds and prevent further forward movement of southwest moisture transport, mainly contributing to the enhancement of moisture convergence. Thus, the anomalous northern SCS cyclonic circulation plays an important role in the moisture transport over HMs.

Analysis of the quasi-geostrophic omega equation reveals that the anomalous ascending motion over HMs is mainly caused by the advection of anomalous temperature by basic zonal winds. Because of the westward increase of temperature anomalies, basic westerly winds prevailing over the north of  $27^\circ\text{N}$  cause warm advection over HMs, which further leads to ascending motions. The anomalous temperature corresponds well with the anomalous circulation, which shows the barotropic structure. It also indicates the importance of circulation anomalies in influencing the precipitation over HMs.

The tropical SST anomalies cause the anomalous lower level SCS cyclone. There exhibits a dipole structure of SST anomalies over the Pacific, with cooling over the equatorial CEP, and warming over the western Pacific and

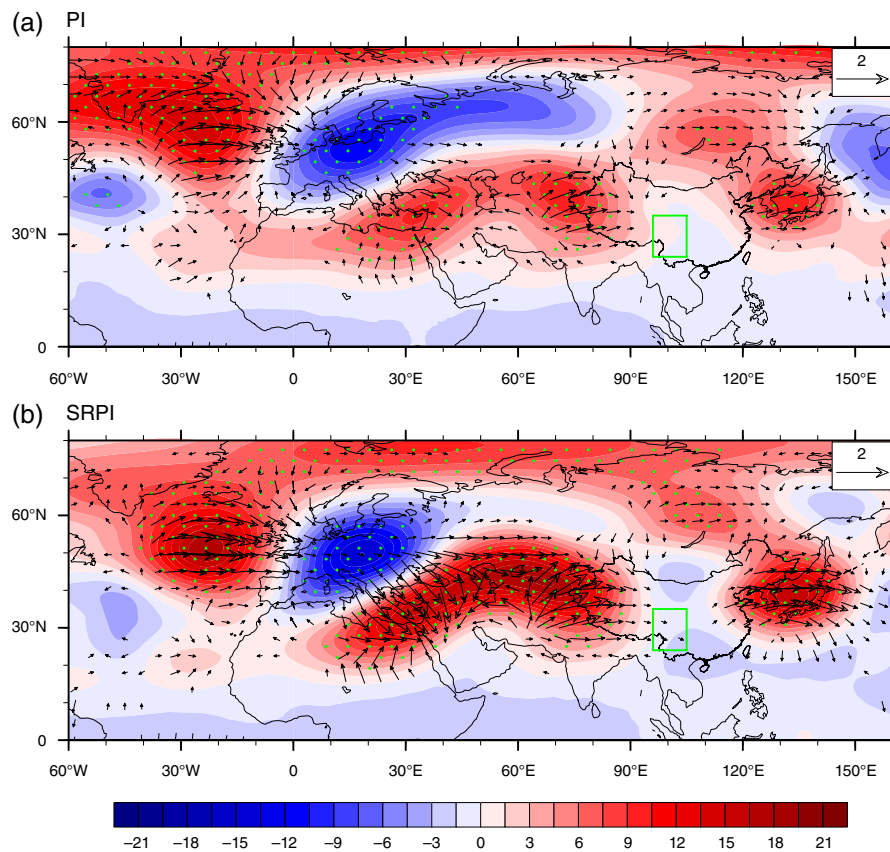


Figure 12. Regression of 200 hPa geopotential height (gpm) and the wave activity fluxes (vectors;  $\text{m}^2 \text{s}^{-2}$ ) with respect to (a) PI and (b) SRPI during rainy season. Dots indicate that the significant level reaches 90%. Arrows with magnitudes  $<0.2$  are omitted. [Colour figure can be viewed at [wileyonlinelibrary.com](http://wileyonlinelibrary.com)].

Table 2. Classification of years in which CEP SST anomalies, SRP, and both of them influence the high and low HMs rainfall.

	High PI	Low PI
CEPI	1990, 1991	None
SRPI	1999, 2007	None
CEPI and SRPI	1984, 1985, 1995, 2001, 2013	1982, 1983, 1987, 1992, 2009

All years are selected based on the 0.8 standard deviation for all the three indices.

much of the northern and southern Pacific. This CEP cooling induces lower (upper) level divergence (convergence) over the CEP and then the descending motions and negative precipitation anomalies. As the adjustment of Walker Circulation, there are ascending motions and positive precipitation anomalies with lower (upper) level convergence (divergence) over the SCS and Maritime Continent. The anomalous SCS cyclone is triggered as a warm Rossby wave response to the positive precipitation anomalies.

The pattern of geopotential height anomalies shows a zonal teleconnection from the North Atlantic Ocean to East Asia, and is highly related to SRP. Due to the barotropic structure of SRP, the geopotential height anomalies correspond well with the temperature anomalies, causing warm and cold anomalies over the central Asia and the central China, respectively. Thus, the basic westerlies

bring warm advection to HMs, leading to the anomalous ascending motions. Figure 13 gives the schematic diagram, illustrating that the effect of the CEP cooling and SRP influence on the circulation anomalies and further HMs precipitation during rainy season.

This study emphasizes the combined effect of the CEP cooling and SRP on the variation of HMs precipitation during rainy season. The results achieved here imply that more attention should be paid on the relationship between the SRP and tropical SST anomalies. The role of the SST anomalies, particularly associated with ENSO, on the SRP is also controversial. Some studies revealed that the SRP is more likely to occur in ENSO developing summer (Ding *et al.*, 2011), and some found that the SRP-ENSO relationship is vague (Yasui and Watanabe, 2010; Kosaka *et al.*, 2012).

Besides, the rainy season over HMs in this study is from May to September. There may exist intraseasonal variation during the whole rainy season. Previous studies have detected significant intraseasonal signals over the TP (e.g. Nitta, 1983; Fujinami and Yasunari, 2004; Yamada and Uyeda, 2006; Zhang *et al.*, 2014b; Wang and Duan, 2015), where adjoins the HMs. Recently, Yang *et al.* (2017) found that the intraseasonal variation of summertime rainfall over the Eastern TP has two dominant peaks centred on quasi-biweekly (12–24) days and quasi-9 (8–11) days. Both of these two oscillations are related to

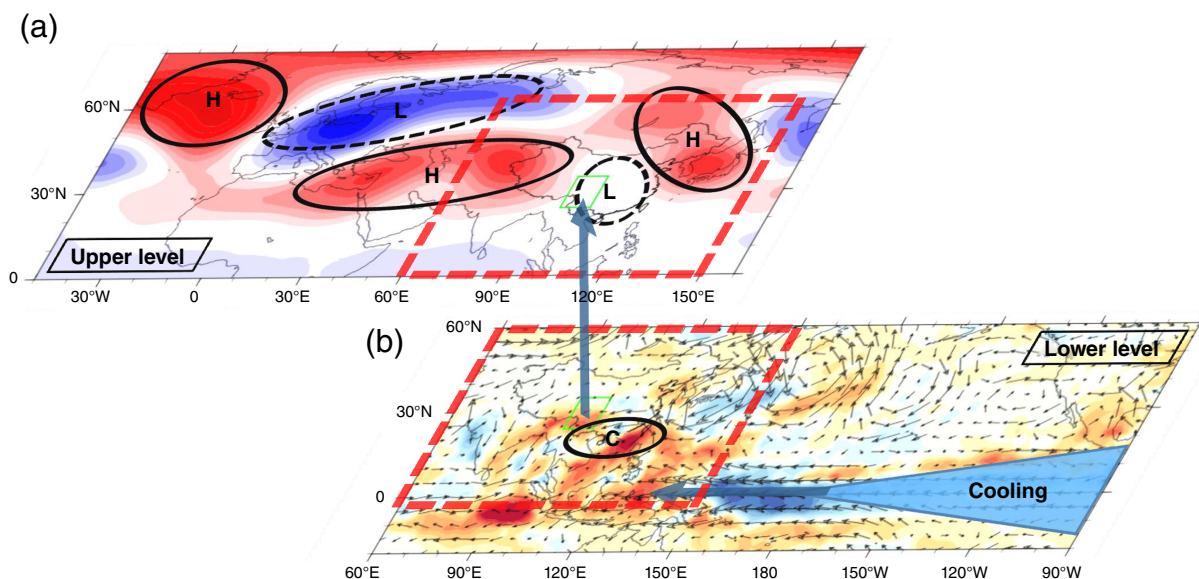


Figure 13. Schematic diagrams illustrating the processes of CEP cooling (b) and SRP (a) influence on the precipitation over HMs during rainy season. The bottom panel shows the PI regressed anomalies of precipitation (shaded; mm) and 700 hPa horizontal wind (vector;  $\text{m s}^{-1}$ ). Panel (a) shows the PI regressed anomalies of geopotential height (gpm). The box represents the HMs region. The shading over the CEP represents negative SST anomalies. The horizontal arrow represents the CEP cooling induced wind anomaly. The ascending arrow represents anomalous ascending motions. The 'C' in black circle represents the anomalous SCS cyclone in the lower level. The 'H' and 'L' in black circle represent anomalous high and low in the upper level. [Colour figure can be viewed at [wileyonlinelibrary.com](http://wileyonlinelibrary.com)].

the mid-latitude wave train at the upper level and tropical wave train at the lower level. Due to that the Eastern TP and HMs have some overlap, their results have a good indication for us to study the intraseasonal variation of precipitation over the HMs during rainy season. Furthermore, whether the interannual variation in the intensity of intraseasonal oscillations over the HMs has an important impact on the precipitation? Thus, more investigations on these issues are needed in the future.

### Acknowledgements

We thank the three anonymous reviewers as well as the editor for their useful comments. This work was supported by the National Outstanding Youth Science Fund Project of China (41425019), the National Natural Science Foundation of China (41721004, 41661144016 and 41705068), the Public Science and Technology Research Funds Projects of Ocean (201505013), and the China Postdoctoral Science Foundation (2016LH0005 and 2016M600116).

### References

- Ban J, Miao Q, Li X. 2006. Analysis of characteristics of temperature variations in Southwest China in recent 50 years. *Resour. Environ. Yangtze Basin* **15**(3): 346–351 (in chinese).
- Bothe O, Fraedrich K, Zhu X. 2010. The large-scale circulations and summer drought and wetness on the Tibetan plateau. *Int. J. Climatol.* **30**(6): 844–855. <https://doi.org/10.1002/joc.1946>.
- Bothe O, Fraedrich K, Zhu X. 2011. Large-scale circulations and Tibetan plateau summer drought and wetness in a high-resolution climate model. *Int. J. Climatol.* **31**(6): 832–846. <https://doi.org/10.1002/joc.2124>.
- Chang C-P, Zhang Y, Li T. 2000. Interannual and interdecadal variations of the East Asian summer monsoon and tropical Pacific SSTs. Part I: roles of the subtropical ridge. *J. Clim.* **13**(24): 4310–4325. [https://doi.org/10.1175/1520-0442\(2000\)013<4310:iaivot>2.0.co;2](https://doi.org/10.1175/1520-0442(2000)013<4310:iaivot>2.0.co;2).
- Chen G, Huang R. 2012. Excitation mechanisms of the teleconnection patterns affecting the July precipitation in northwest China. *J. Clim.* **25**(22): 7834–7851. <https://doi.org/10.1175/jcli-d-11-00684.1>.
- Chen T-C, Tzeng R-Y. 1990. Global-scale intraseasonal and annual variation of divergent water-vapor flux. *Meteorol. Atmos. Phys.* **44**(1): 133–151. <https://doi.org/10.1007/bf01026815>.
- Chen Z, Wen Z, Wu R, Lin X, Wang J. 2016. Relative importance of tropical SST anomalies in maintaining the Western North Pacific anomalous anticyclone during El Niño to La Niña transition years. *Clim. Dyn.* **46**(3): 1027–1041. <https://doi.org/10.1007/s00382-015-2630-1>.
- Chowdary JS, Harsha HS, Gnanaseelan C, Srinivas G, Parekh A, Pillai P, Naidu CV. 2016a. Indian summer monsoon rainfall variability in response to differences in the decay phase of El Niño. *Clim. Dyn.* **48**: 2707–2727. <https://doi.org/10.1007/s00382-016-3233-1>.
- Chowdary JS, Parekh A, Kakatkar R, Gnanaseelan C, Srinivas G, Singh P, Roxy MK. 2016b. Tropical Indian Ocean response to the decay phase of El Niño in a coupled model and associated changes in south and east-Asian summer monsoon circulation and rainfall. *Clim. Dyn.* **47**(3): 831–844. <https://doi.org/10.1007/s00382-015-2874-9>.
- Dee DP, Uppala SM, Simmons AJ, Berrisford P, Poli P, Kobayashi S, Andrae U, Balmaseda MA, Balsamo G, Bauer P, Bechtold P, Beljaars ACM, van de Berg L, Bidlot J, Bormann N, Delsol C, Dragani R, Fuentes M, Geer AJ, Haimberger L, Healy SB, Hersbach H, Hólm EV, Isaksen L, Kållberg P, Köhler M, Matricardi M, McNally AP, Monge-Sanz BM, Morcrette JJ, Park BK, Peubey C, de Rosnay P, Tavolato C, Thépaut JN, Vitart F. 2011. The ERA-Interim reanalysis: configuration and performance of the data assimilation system. *Q. J. R. Meteorol. Soc.* **137**(656): 553–597. <https://doi.org/10.1002/qj.828>.
- Ding Q, Wang B. 2005. Circumglobal teleconnection in the northern hemisphere summer. *J. Clim.* **18**(17): 3483–3505. <https://doi.org/10.1175/jcli3473.1>.
- Ding Q, Wang B, Wallace JM, Branstator G. 2011. Tropical–extratropical teleconnections in boreal summer: observed interannual variability. *J. Clim.* **24**(7): 1878–1896. <https://doi.org/10.1175/2011jcli3621.1>.
- Dong W, Lin Y, Wright JS, Ming Y, Xie Y, Wang B, Luo Y, Huang W, Huang J, Wang L, Tian L, Peng Y, Xu F. 2016. Summer rainfall over the southwestern Tibetan plateau controlled by deep convection

- over the Indian subcontinent. *Nat. Commun.* **7**: 10925. <https://doi.org/10.1038/ncomms10925>.
- Enomoto T, Hoskins BJ, Matsuda Y. 2003. The formation mechanism of the Bonin high in August. *Q. J. R. Meteorol. Soc.* **129**(587): 157–178. <https://doi.org/10.1256/qj.01.211>.
- Fujinami H, Yasunari T. 2004. Submonthly variability of convection and circulation over and around the Tibetan plateau during the boreal summer. *J. Meteorol. Soc. Jpn Ser. II* **82**(6): 1545–1564. <https://doi.org/10.2151/jmsj.82.1545>.
- Gao Y, Wang H, Li S. 2013. Influences of the Atlantic Ocean on the summer precipitation of the southeastern Tibetan plateau. *J. Geophys. Res. Atmos.* **118**(9): 3534–3544. <https://doi.org/10.1002/jgrd.50290>.
- Hong X, Lu R. 2016. The Meridional displacement of the Summer Asian Jet, Silk Road pattern, and tropical SST anomalies. *J. Clim.* **29**(10): 3753–3766. <https://doi.org/10.1175/JCLI-D-15-0541.1>.
- Hoskins BJ, Ambrizzi T. 1993. Rossby wave propagation on a realistic longitudinally varying flow. *J. Atmos. Sci.* **50**(12): 1661–1671. [https://doi.org/10.1175/1520-0469\(1993\)050<1661:rwpoar>2.0.co;2](https://doi.org/10.1175/1520-0469(1993)050<1661:rwpoar>2.0.co;2).
- Huang R, Zhang Z, Huang G, Ren B. 1998. Characteristics of the water vapor transport in East Asian monsoon region and its differences from that of South Asian monsoon region in summer. *Sci. Atmos. Sin.* **22**: 368–379.
- Huang G, Liu Y, Huang R. 2011. The interannual variability of summer rainfall in the arid and semiarid regions of Northern China and its association with the northern hemisphere circumglobal teleconnection. *Adv. Atmos. Sci.* **28**(2): 257–268. <https://doi.org/10.1007/s00376-010-9225-x>.
- Huang B, Banzon VF, Freeman E, Lawrimore J, Liu W, Peterson TC, Smith TM, Thorne PW, Woodruff SD, Zhang H-M. 2015. Extended Reconstructed Sea Surface Temperature version 4 (ERSST.v4). Part I: upgrades and intercomparisons. *J. Clim.* **28**(3): 911–930. <https://doi.org/10.1175/jcli-d-14-00006.1>.
- Kosaka Y, Nakamura H, Watanabe M, Kimoto M. 2009. Analysis on the dynamics of a wave-like teleconnection pattern along the summertime Asian Jet based on a reanalysis dataset and climate model simulations. *J. Meteorol. Soc. Jpn* **87**(3): 561–580. <https://doi.org/10.2151/jmsj.87.561>.
- Kosaka Y, Chowdary JS, Xie S-P, Min Y-M, Lee J-Y. 2012. Limitations of seasonal predictability for summer climate over east Asia and the northwestern Pacific. *J. Clim.* **25**(21): 7574–7589. <https://doi.org/10.1175/jcli-d-12-00009.1>.
- Li Z, He Y, Wang C, Wang X, Xin H, Zhang W, Cao W. 2011. Spatial and temporal trends of temperature and precipitation during 1960–2008 at the Hengduan Mountains, China. *Quat. Int.* **236**(1–2): 127–142. <https://doi.org/10.1016/j.quaint.2010.05.017>.
- Lin Z. 2014. Intercomparison of the impacts of four summer teleconnections over Eurasia on East Asian rainfall. *Adv. Atmos. Sci.* **31**(6): 1366–1376. <https://doi.org/10.1007/s00376-014-3171-y>.
- Liu X, Yin Z-Y. 2001. Spatial and temporal variation of summer precipitation over the eastern Tibetan plateau and the north Atlantic oscillation. *J. Clim.* **14**(13): 2896–2909. [https://doi.org/10.1175/1520-0442\(2001\)014<2896:satvos>2.0.co;2](https://doi.org/10.1175/1520-0442(2001)014<2896:satvos>2.0.co;2).
- Lu R-Y, Oh J-H, Kim B-J. 2002. A teleconnection pattern in upper-level meridional wind over the North African and Eurasian continent in summer. *Tellus A* **54**(1): 44–55. <https://doi.org/10.1034/j.1600-0870.2002.00248.x>.
- Ma Z, Peng J, Gao W, Tian H. 2006. Climate variation of Southwest China in recent 40 Years. *Plateau Meteorol.* **25**(4): 633–642 (in chinese).
- Nie ZL, Gu ZJ, Sun H. 2002. Cytological study of Tibetia (Fabaceae) in the Hengduan Mountains region, China. *J. Plant Res.* **115**(1): 0017–0022. <https://doi.org/10.1007/s102650200003>.
- Nitta T. 1983. Observational study of heat sources over the eastern Tibetan plateau during the summer monsoon. *J. Meteorol. Soc. Jpn Ser. II* **61**(4): 590–605. [https://doi.org/10.2151/jmsj1965.61.4\\_590](https://doi.org/10.2151/jmsj1965.61.4_590).
- Peixoto JP, Oort AH. 1984. Physics of climate. *Rev. Mod. Phys.* **56**(3): 365–429.
- Qin N, Chen X, Fu G, Zhai J, Xue X. 2010. Precipitation and temperature trends for the Southwest China: 1960–2007. *Hydrol. Process.* **24**(25): 3733–3744. <https://doi.org/10.1002/hyp.7792>.
- Qu X, Huang G, Hu K, Xie S-P, Du Y, Zheng X-T, Liu L. 2015. Equatorward shift of the South Asian high in response to anthropogenic forcing. *Theor. Appl. Climatol.* **119**(1–2): 113–122. <https://doi.org/10.1007/s00704-014-1095-1>.
- Sato N, Takahashi M. 2003. Formation mechanism of vorticity anomalies on the subtropical jet in the midsummer northern hemisphere. *Theor. Appl. Mech.* **52**: 109–115. <https://doi.org/10.11345/nctam.52.109>.
- Tao W, Huang G, Wu R, Hu K, Wang P, Chen D. 2016. Asymmetry in summertime atmospheric circulation anomalies over the northwest Pacific during decaying phase of El Niño and La Niña. *Clim. Dyn.* **49**: 2007–2023. <https://doi.org/10.1007/s00382-016-3432-9>.
- Trenberth KE. 1991. Climate diagnostics from global analyses: conservation of mass in ECMWF analyses. *J. Clim.* **4**(7): 707–722. [https://doi.org/10.1175/1520-0442\(1991\)004<0707:cdfgac>2.0.co;2](https://doi.org/10.1175/1520-0442(1991)004<0707:cdfgac>2.0.co;2).
- Wang M, Duan A. 2015. Quasi-biweekly oscillation over the Tibetan plateau and its link with the Asian summer monsoon. *J. Clim.* **28**(12): 4921–4940. <https://doi.org/10.1175/jcli-d-14-00658.1>.
- Wang L, Wu R. 2012. In-phase transition from the winter monsoon to the summer monsoon over East Asia: role of the Indian Ocean. *J. Geophys. Res. Atmos.* **117**(D11): D11112. <https://doi.org/10.1029/2012JD017509>.
- Wang B, Zhang Q. 2002. Pacific-East Asian teleconnection. Part II: how the Philippine Sea anomalous anticyclone is established during El Niño development. *J. Clim.* **15**(22): 3252–3265. [https://doi.org/10.1175/1520-0442\(2002\)015<3252:peatpi>2.0.co;2](https://doi.org/10.1175/1520-0442(2002)015<3252:peatpi>2.0.co;2).
- Wang B, Wu R, Fu X. 2000. Pacific-East Asian teleconnection: how does ENSO affect East Asian climate? *J. Clim.* **13**(9): 1517–1536. [https://doi.org/10.1175/1520-0442\(2000\)013<1517:peatpd>2.0.co;2](https://doi.org/10.1175/1520-0442(2000)013<1517:peatpd>2.0.co;2).
- Wang B, Xiang B, Lee J-Y. 2013. Subtropical high predictability establishes a promising way for monsoon and tropical storm predictions. *Proc. Natl. Acad. Sci. U.S.A.* **110**(8): 2718–2722. <https://doi.org/10.1073/pnas.1214626110>.
- Wei W, Zhang R, Wen M, Rong X, Li T. 2014. Impact of Indian summer monsoon on the South Asian High and its influence on summer rainfall over China. *Clim. Dyn.* **43**(5): 1257–1269. <https://doi.org/10.1007/s00382-013-1938-y>.
- Wu R. 2002. A mid-latitude Asian circulation anomaly pattern in boreal summer and its connection with the Indian and East Asian summer monsoons. *Int. J. Climatol.* **22**(15): 1879–1895. <https://doi.org/10.1002/joc.845>.
- Wu R, Hu Z-Z, Kirtman BP. 2003. Evolution of ENSO-related rainfall anomalies in east Asia. *J. Clim.* **16**(22): 3742–3758. [https://doi.org/10.1175/1520-0442\(2003\)016<3742:eoerai>2.0.co;2](https://doi.org/10.1175/1520-0442(2003)016<3742:eoerai>2.0.co;2).
- Wu B, Zhou T, Li T. 2009. Seasonally evolving dominant interannual variability modes of East Asian climate. *J. Clim.* **22**(11): 2992–3005. <https://doi.org/10.1175/2008jcli2710.1>.
- Xiang B, Wang B, Yu W, Xu S. 2013. How can anomalous western north Pacific subtropical high intensify in late summer? *Geophys. Res. Lett.* **40**(10): 2349–2354. <https://doi.org/10.1002/grl.50431>.
- Xiao C, Yu R, Yuan W, Li J. 2013. Characteristics of the seasonal evolution of precipitation over the central western part of the Henghuan Mountain. *Acta Meteorol. Sin.* **71**(4): 643–651 (in chinese).
- Xie P, Arkin PA. 1997. Global precipitation: a 17-year monthly analysis based on gauge observations, satellite estimates, and numerical model outputs. *Bull. Am. Meteorol. Soc.* **78**(11): 2539–2558. [https://doi.org/10.1175/1520-0477\(1997\)078<2539:gpayma>2.0.co;2](https://doi.org/10.1175/1520-0477(1997)078<2539:gpayma>2.0.co;2).
- Xie S-P, Zhou Z-Q. 2017. Seasonal modulations of El Niño-related atmospheric variability: Indo-western Pacific ocean feedback. *J. Clim.* **30**: 3461–3472. <https://doi.org/10.1175/jcli-d-16-0713.1>.
- Xie S-P, Hu K, Hafner J, Tokinaga H, Du Y, Huang G, Sampe T. 2009. Indian Ocean capacitor effect on Indo-Western Pacific climate during the summer following El Niño. *J. Clim.* **22**(3): 730–747. <https://doi.org/10.1175/2008jcli2544.1>.
- Xie S-P, Kosaka Y, Du Y, Hu K, Chowdary JS, Huang G. 2016. Indo-western Pacific ocean capacitor and coherent climate anomalies in post-ENSO summer: a review. *Adv. Atmos. Sci.* **33**(4): 411–432. <https://doi.org/10.1007/s00376-015-5192-6>.
- Yamada H, Uyeda H. 2006. Transition of the rainfall characteristics related to the moistening of the land surface over the central Tibetan plateau during the summer of 1998. *Mon. Weather Rev.* **134**(11): 3230–3247. <https://doi.org/10.1175/mwr3235.1>.
- Yang J, Liu Q, Xie S-P, Liu Z, Wu L. 2007. Impact of the Indian Ocean SST basin mode on the Asian summer monsoon. *Geophys. Res. Lett.* **34**(2): L02708. <https://doi.org/10.1029/2006GL028571>.
- Yang J, Liu Q, Liu Z. 2010. Linking observations of the Asian monsoon to the Indian Ocean SST: possible roles of Indian Ocean basin mode and dipole mode. *J. Clim.* **23**(21): 5889–5902. <https://doi.org/10.1175/2010jcli2962.1>.
- Yang J, Bao Q, Wang B, He H, Gao M, Gong D. 2017. Characterizing two types of transient intraseasonal oscillations in the Eastern Tibetan Plateau summer rainfall. *Clim. Dyn.* **48**(5): 1749–1768. <https://doi.org/10.1007/s00382-016-3170-z>.
- Yasui S, Watanabe M. 2010. Forcing processes of the summertime circumglobal teleconnection pattern in a dry AGCM. *J. Clim.* **23**(8): 2093–2114. <https://doi.org/10.1175/2009jcli3323.1>.
- Zhang R, Sumi A, Kimoto M. 1996. Impact of El Niño on the East Asian monsoon: a diagnostic study of the '86/87 and '91/92 events. *J. Meteorol. Soc. Jpn* **74**(1): 49–62.

- Zhang P, Li G, Fu X, Liu Y, Li L. 2014a. Clustering of Tibetan plateau vortices by 10–30-day intraseasonal oscillation. *Mon. Weather Rev.* **142**(1): 290–300. <https://doi.org/10.1175/mwr-d-13-00137.1>.
- Zhang K, Pan S, Cao L, Wang Y, Zhao Y, Zhang W. 2014b. Spatial distribution and temporal trends in precipitation extremes over the Hengduan Mountains region, China, from 1961 to 2012. *Quat. Int.* **349**: 346–356. <https://doi.org/10.1016/j.quaint.2014.04.050>.
- Zhang T, Li B, He Y, Du J, Niu H, Xin H. 2015. Spatial and temporal distribution of precipitation based on corrected TRMM data in Hengduan Mountains. *J. Nat. Resour.* **30**(4): 260–270. <https://doi.org/10.11849/zrzyxb.2015.02.009> (in chinese).
- Zhao G, Huang G, Wu R, Tao W, Gong H, Qu X, Hu K. 2015. A new upper-level circulation index for the East Asian summer monsoon variability. *J. Clim.* **28**(24): 9977–9996. <https://doi.org/10.1175/JCLI-D-15-0272.1>.
- Zhu G, Pu T, Zhang T, Liu H, Zhang X, Liang F. 2013. The accuracy of TRMM precipitation data in Hengduan Mountainous Region, China. *Sci. Geogr. Sin.* **33**(9): 1125–1131. <https://doi.org/10.13249/j.cnki.sgs.2013.09.015> (in chinese).
- Zhu G, Qin D, Tong H, Liu Y, Li J, Chen D, Wang K, Hu P. 2016. Variation of Thornthwaite moisture index in Hengduan Mountains, China. *Chin. Geogr. Sci.* **26**(5): 687–702. <https://doi.org/10.1007/s11769-016-0820-3>.